Rock lithological classification by hyperspectral, range 3D and color images

Francisco J. Galdames [*], Claudio A. Perez, Pablo A. Estévez, Martin Adams

Advanced Mining Technology Center (AMTC) and Department of Electrical Engineering, Universidad de Chile, Av. Tupper 2007, Santiago, Chile

ABSTRACT

Mine operations in the future will require automatic rock characterization at many different stages, since it can be used to supervise and optimize various processes in the laboratory as well as at the mine locations for planning and exploitation. Different methods for classifying rocks based on image analysis have been proposed in the past. In this paper, we report the use of hyperspectral sensors in the classification of rock lithology. The lithology provides information about the chemical composition of the rock, and its physical properties. According to our literature review, this is the first time hyperspectral sensors have been employed in rock type classification. Additionally, it is the first time the use of three different technologies in rock type classification has been reported: hyperspectral sensors, laser range and a color camera. We use two hyperspectral sensors, one has sensibility within the visible and near-infrared range of 400–1000 nm, and the second has sensibility within the short-wavelength infrared range of 900–2500 nm. The range and high definition color images are used to perform accurate segmentation of the rock samples. Images are tessellated into sub-images in which various features from the three sensor types are extracted. In a first stage, the sub-images are classified by using a support-vector machine (SVM) classifier with the extracted features as inputs. In a second stage, the rock segmentation is used to perform a voting process among all the sub-images of each rock and improve the classification. The method was tested using a database with 13 lithologies from a copper mine in Chile. The results show that lithological classification performance obtained by using hyperspectral images greatly exceeds the performance of the color and range images. The achieved classification performance was 98.62% using sub-image classification and 99.95% using a voting process among sub-images. The number of features was also reduced by using the CMIM (Conditional Mutual Information Maximization) feature selection method, achieving a performance of over 99% with using only 3% of the total number of features.

1. Introduction

Rock type classification is very useful in many stages of mine operations. This classification can be used from the mine planning to the control of various processes, for example, the grinding [1,2] which consumes about 50% of the energy used in a mining plant. Information about the rock types and hardness can be used in controlling the feeding and speed of the mill, optimizing the energy consumption, processing the ore [3,4], and reducing CO_2 emissions. The classification and characterization of rocks is usually carried out visually by geologists and mineralogists, or by performing laboratory tests [2]. However, manual classification is time-consuming, and sometimes it is necessary to stop the ore processing in order to perform it. Moreover, manual classification yields only a coarse approximation, since it is usually carried out using a small number of samples.

It is desirable to develop a technology for automatic rock classification that would enable monitoring rock type continuously at any stage of the mine operation [3]. Several attempts to develop such a technology have been done in the past two decades. A method based on color images and neural networks (NNs) to classify seven rock types was developed almost two decades ago, as reported in Ref. [5]. Later, extracted features from color images were selected using genetic algorithms as inputs to a NN which improved classification results slightly [1].

In Ref. [6] a rock classification system combining texture information and co-occurrence likelihoods were introduced. A rock classification technique using Gabor filtering with various color spaces was developed in Ref. [7]. Histogram processing using RGB channels and texture analysis based on the co-occurrence matrix on gray levels, together with edge detection for the classification of ferruginous manganese ore was performed in Ref. [8]. Later, a pilot plant was created to estimate the rock

type composition mixture for classifying five different minerals using an SVM, Principal Component Analysis (PCA), and Wavelet Texture Analysis (WTA) to extract color and textural features [4].

Classification of 26 rock types was reported in Ref. [9] who used a PCA and frequency components in a NN. Another study used a hierarchical neuro-fuzzy model for the classification of rock textures [10]. Later, using genetic algorithms, *k*-means clustering, and NNs, the ore grade was determined in samples extracted from a drill-hole in a lead-zinc deposit as described in Refs. [2,11]. The texture of various basalts in RGB and gray scale images was determined using NN in Ref. [12]. Granite tiles with rotations were classified by measurements using different types of Local Binary Patterns (LBP), Improved Local Binary Patterns (ILBP), and Coordinated Cluster Representation (CCR) with the best results achieved with ILBPs [13]. In another application the Hu and Zernike moments were extracted from segmented rocks, and classification was performed by a NN [14]. Perez [15] used a multi-way PCA to extract color features, and a WTA to extract texture features from a database of various rock types. The method selected the most relevant features and used an SVM to classify sub-images by using mutual information. Rock type classification was improved by a voting process among all classified sub-images within the rock boundary. More recently, this rock type classification system was improved by adding multi-scale Gabor filters to extract features [16]. Another application was developed for the classification of granite tiles and reached the best performance with the co-occurrence matrix [17]. Limestone rock-types were classified using histogram based features from color images and probabilistic NNs in Ref. [18]. More recently, texture features computed in range and color images were used to perform rock lithological classification in Ref. [19].

Multi- and hyper-spectral images show the electromagnetic emissions of different wavelengths in the electromagnetic spectrum. Color (RGB) images are considered to be multi-spectral images with 3 channels (red, green, blue) within the visible light range of 400–750 nm. It is intuitive to think that better results in rock classification could be obtained by using more than 3 channels. Hyperspectral images have been used to identify many types of materials [20,21]. For example, the use of hyperspectral images in the near-infrared and visible spectrum to predict the properties of extruded wood/plastic composite materials was reported in Ref. [22]. Also, hyperspectral images have been used for detecting damage on potatoes [23] and apples [24], or for classifying coffee species [25,26]. The presence of specific minerals can be detected by their "hyperspectral signature". Multi- and hyper-spectral images can be acquired remotely [27] or at a microscopic level [28] to identify the minerals present in a zone or in an ore sample, respectively.

In Ref. [29] a nearest-subspace classification (NSC) method with distance-weighted Tikhonov regularization was proposed for hyperspectral classification of aerial images. Spatial features computed with Gabor filters were incorporated in the method by Ref. [30]. In Ref. [31], a dictionary optimized by a task-driven formulation was used to classify images acquired with airborne sensors. The method used Laplacian regularization to incorporate spatial information. Joint robust sparse representation-based classification (JRSRC) was introduced in Ref. [32], and tested in aerial images. The method can handle outliers and takes the neighborhood around the pixel into account in the classification.

In Ref. [33], a convolutional neural networks was used to classify the pixels of airborne hyperspectral data sets using the original data as input. A deep NN with two branches was used to compute spectral-spatial features and classify aerial images in Ref. [34]. In Ref. [35], a joint sparse and low-rank multitask learning (MTL) method with Laplacian-like regularization, named sllMTL, was proposed. The method incorporates morphological operators to compute the features, and was tested on aerial hyperspectral images. A method that uses features based on a 2D variational mode decomposition, (2-D-VMD), and a kernel low-rank MTL (KL-MTL) classifier was presented in Ref. [36].

In mining, multispectral information has been used to classify and analyze drill cores. In Ref. [37], a method based on spectroscopy in the visible and IR spectrum was developed to determine the mineralogy and lithology of drill core pulps, and achieved results similar to those obtained using X-Ray diffraction. A system, called multi-sensor core logger (MSCL), for acquiring data from drill rock cores used in mineral exploration was presented in Ref. [38]. The system can acquire data of volumetric magnetic susceptibility, density using gamma-ray attenuation, and several chemical elements through energy-dispersive X-ray fluorescence spectrometry, and visible/near infrared spectrometry. The HyLogger developed by CSIRO is a similar system used in drill cores, which incorporates a laser profilometer and can capture high color images and one-dimensional hyperspectral scans [39–41].

In this paper, we report the use of hyperspectral sensors in the classification of rock type. According to our literature review, this is the first time hyperspectral sensors have been employed in rock type classification. Additionally, it is the first time the use of three different technologies in rock type classification is reported: hyperspectral sensors, color camera, and laser 3D range camera. More specifically, we use the hyperspectral sensor, VNIR, with sensibility within the visible and near-infrared range of 400–1000 nm, and the SWIR sensor with sensibility within the short-wavelength infrared range of 900–2500 nm. Captured images within these spectral ranges are combined with range and high definition color images to perform segmentation of the rock samples. Images are tessellated into sub-images in which various features are extracted. In the color and range images, features based on Gabor filters and Local Binary Patterns (LBP) are computed within each sub-image. In the hyperspectral images, the mean and standard deviation inside each channel of the sub-images are used as features. The features are computed on the same sub-images of images coming from the different sensors, and the features are concatenated to build a feature vector. The rock lithology for each sub-image is determined by using a support-vector machine (SVM) classifier. Then, using the rock segmentation, a voting process among all the sub-images of each rock is used to improve rock classification. The method is validated on a database with 13 different rock lithologies. Results proved to be significantly better than previous results had been on the same database.

2. Materials

2.1. Color-range, hyperspectral VNIR, and hyperspectral SWIR image acquisition

In order to improve our previous method of lithological classification of rock types based on color and range images [19], two hyperspectral cameras were used to acquire rock images.

We use a SICK ColorRange Ranger-E55444 for color and laser range image acquisition. This camera acquires 3D range images using a laser and a high-definition color image. The camera, using a CMOS sensor, acquires the range images, line by line, as objects move. Three lines of the CMOS sensor are employed in acquiring the red, green, and blue channels for the high resolution color images. Each line has a resolution of 3072 columns. The same sensor has another 411 lines, each one with a resolution of 1536 columns that are used for creating the range image using an infrared (IR) laser. The IR laser was mounted at 45° relative to the surface of a camera dolly on which the rocks lay. A line that is projected by the IR laser is deformed by the rocks on the dolly. This deformation is captured by the CMOS sensor with an IR filter. Then, using a previous calibration and the laser line deformation, a 3D surface of the rocks is computed as the dolly moves.

The first hyperspectral camera is a SPECIM spectral sCMOS camera VNIR[1] (visible and near-infrared) with an ImSpector N10E imaging spectrograph. The camera is equipped with a 23 mm lens and acquires images using 968 wavelengths in the visible and near-infrared region of the electromagnetic spectrum (393–1008 nm). It has a line-scan sensor

---
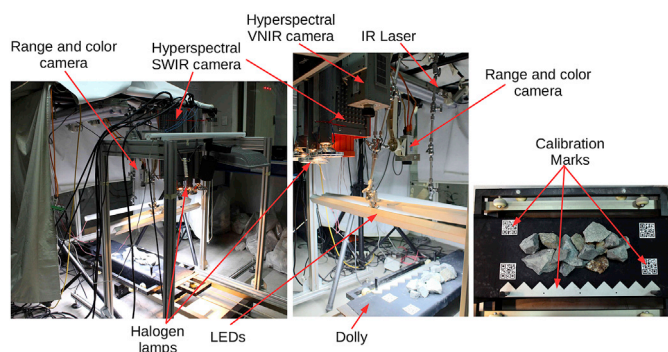
Fig. 1. Acquisition system: Hyperspectral SWIR, hyperspectral VNIR, and a range-color camera mounted together to acquire the four types of images.

Fig. 2. Examples of acquired color, range, hyperspectral VNIR and hyperspectral SWIR images. The red boxes show the computed positions of the marks used to register the images. (a) Color image. (b) Range image. (c) VNIR image, one channel. (d) SWIR image, one channel. (For interpretation of the references to color in this figure legend, the reader is referred to the Web version of this article.)

from which 1064 pixels were used. The second hyperspectral camera is a SPECIM Spectral Camera SWIR[2] (Short-wavelength infrared) with a cryogenically cooled mercury cadmium telluride (MCT) detector. This camera acquires images with 288 wavelengths in the near-infrared region of the electromagnetic spectrum (904–2516 nm). It has a line-scan sensor with 384 pixels.

A camera dolly was used to move the sample rocks under the cameras. Marks visible in the four types of images were placed over the camera dolly to calibrate the cameras and register the images (see Fig. 1 right). Halogen lamps were used for the hyperspectral acquisition, and LEDs were used for the color images. An infrared laser was used for the range acquisition. Fig. 1 shows the acquisition system with the three mounted cameras.
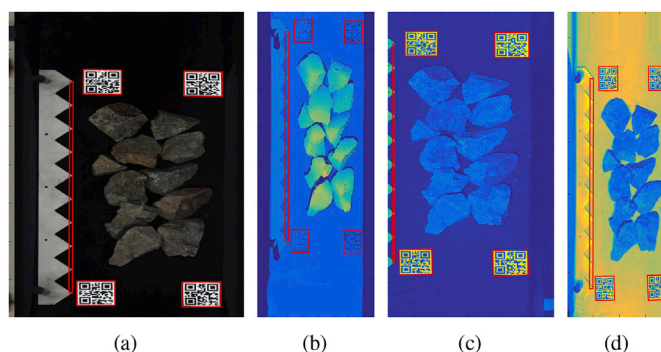
The spectra acquired with both hyperspectral cameras were corrected and transformed to reflectance by using a pixelwise calibration model [42], as follows:

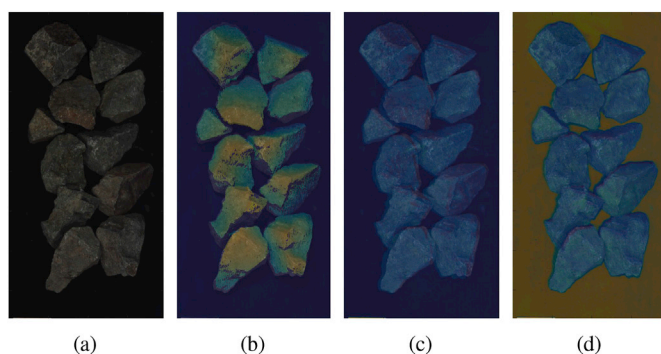$$I(x, y) = \frac{I_0(x, y) - B(x)}{W(x) - B(x)}, \tag{1}$$

where B is a black calibration image, W is a total reflectance image, I_0 is the original hyperspectral image, and I is the corrected image. The black calibration image, B, is acquired to measure the detector dark current by blocking the camera lens after each image acquisition. The total reflectance images, W, were acquired using a surface made of Spectralon. The values $W(x)$ and $B(x)$ are the means of the images along the y axis.

Each type of image has a different resolution. The color image has the highest resolution of 3072 columns, the range image has 1536 columns, the hyperspectral SWIR image has 384 columns, and the hyperspectral VNIR has 1064 columns. The images are not registered. Also, because of the laser triangulation system, the range image must be corrected using the acquisition system geometry and the known location of the registration marks. Two types of marks were used in the acquisition: QR codes, and a tool shaped like a saw. The QR codes are visible in the color, and hyperspectral images, and in the laser intensity image associated with the range images; and the saw is visible in all the image types. In order to calibrate and register the acquired images, the marks must be detected in all the image types. The template matching Correlation Co-efficient method together with the oriented BRIEF (ORB) [43] and the Binary Robust Invariant Scalable Keypoints (BRISK) [44] methods, are used to find the location of the marks in each image. Then, these locations are used to register the images. The transformation used in the registration is computed to have isotropic pixels. Fig. 2 shows examples of the four types of images and the computed position of the marks in each image. Fig. 3 shows the result of the registration.


Fig. 3. Registration of color, range, hyperspectral VNIR and hyperspectral SWIR images. (a) Color image. (b) Color image with the range image superimposed. (c) Color image with one channel of the VNIR image superimposed. (d) Color image with one channel of the SWIR image superimposed. (For interpretation of the references to color in this figure legend, the reader is referred to the Web version of this article.)

Fig. 4 shows different channels of a hyperspectral VNIR image, each channel representing the intensity of the electromagnetic spectrum at a different wavelength. Fig. 5 shows different channels of a hyperspectral SWIR image.
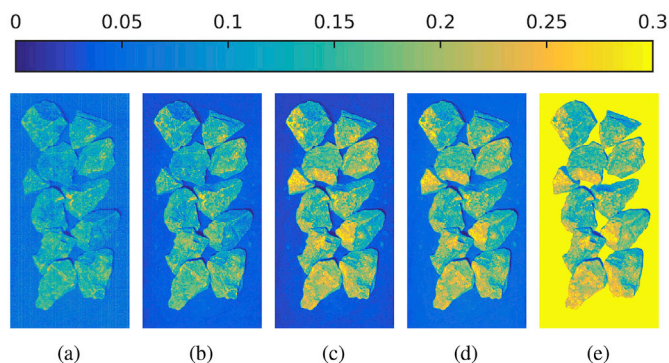
Fig. 4. Examples of the channels of a VNIR image acquired at different wavelengths using the hyperspectral camera. The color scale represents the reflectance. The background color is saturated when exceed the maximum reflectance of the rock samples. The wavelengths in nanometers are: (a) 408.62, (b) 465.46, (c) 620.93, (d) 668.97, (e) 842.57. (For interpretation of the references to color in this figure legend, the reader is referred to the Web version of this article.)
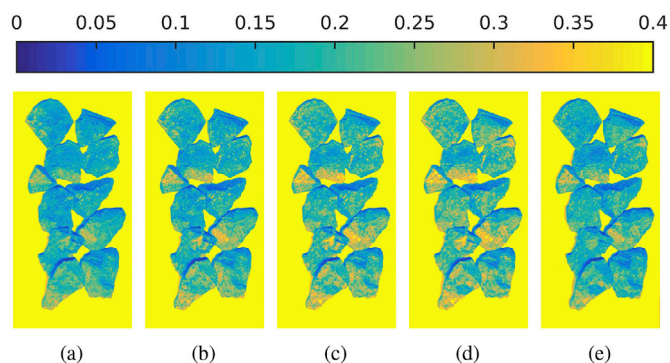
Fig. 5. SWIR image acquired at different wavelengths using the hyperspectral camera. The color scale represents the reflectance. The background color is saturated when exceed the maximum reflectance of the rock samples. The wavelengths in nanometers are: (a) 1039.83, (b) 1356.42, (c) 1750.89, (d) 2126.44, (e) 2349.4. (For interpretation of the references to color in this figure legend, the reader is referred to the Web version of this article.)
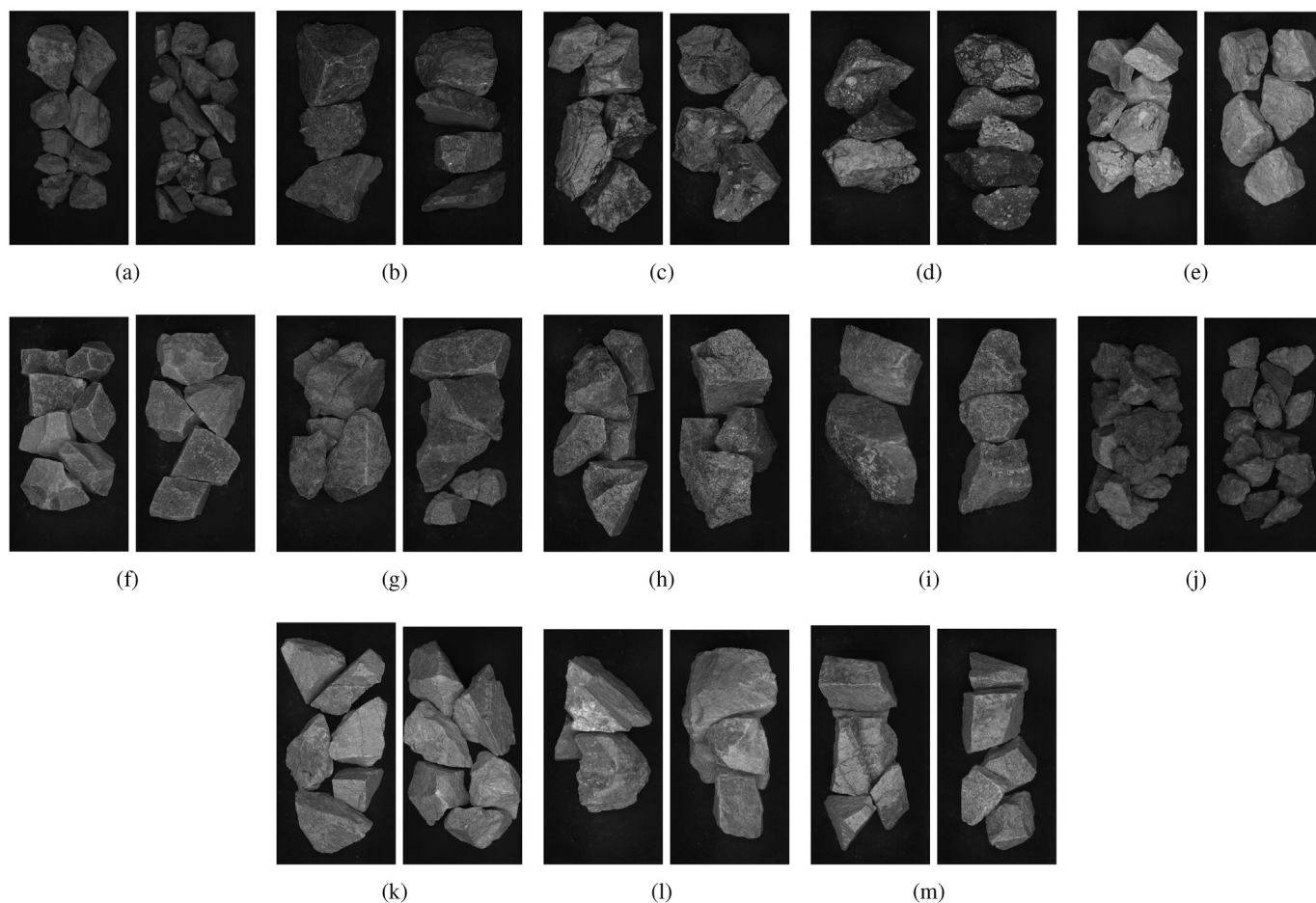
3. Database

A database was built using ore samples of 5 lithologies from a copper mine in Chile [16], and samples of 8 lithologies from the Andina division of Codelco. The lithologies were determined by experts from Andina. The lithologies of the ore samples are: Andesite (site 1); Andesite (site 2); Dacitic Diatreme; Granodiorite Cascada (site); Granodiorite,

Molybdenite, and Primary rock Rio Blanco (site); Granodiorite Rio Blanco (site); Other Breccias; Porphyritic Dykes; Porphyry don Luis (site); Quartz monzonite porphyry; Rhyolitic Diatreme; Tourmaline Breccia; and Tourmaline and Tufa Breccias. Sets of 20 range, color, hyperspectral VNIR, and hyperspectral SWIR images were acquired for these lithologies.

In each image acquisition, various samples were selected and placed in different orientations and positions as in Ref. [2]. Fig. 6 shows sample color images of the 13 lithologies. The sizes of the rock samples are between 4 and 20 cm. Some lithologies have rock samples of grater size than others, and therefore fewer samples of these lithologies can be put in the same image. Nevertheless, the information about the size and the number of samples in each image is not taken into account in the classification method. There are some lithologies in the database that can be differentiated from one another by a non-expert, but in general the precise classification of these lithologies requires expert knowledge. For example, as shown in Fig. 6, samples from Tourmaline Breccia (c) and Tourmaline and Tufa Breccias (d); or Dacitic Diatreme (e) and Porphyritic Dykes (k); are not distinguishable for the non-expert.

4. Methods

Features computed in color, range, and hyperspectral images were tested for lithological classification. Fig. 7 shows a block diagram of the proposed method. The images are tessellated into sub-images to perform the first classification. Features are computed in each sub-image and an SVM is used to classify the lithology of each sub-image. The rocks present

Fig. 6. Color images of the rock database. (a) Andesite (site 1). (b) Andesite (site 2). (c) Tourmaline Breccia. (d) Tourmaline and Tufa Breccias. (e) Dacitic Diatreme. (f) Rhyolitic Diatreme. (g) Granodiorite Cascada (site). (h) Granodiorite Rio Blanco (site). (i) Granodiorite, Molybdenite and Primary rock Rio Blanco (site). (j) Other Breccias. (k) Porphyritic Dykes. (l) Porphyry don Luis (site). (m) Quartz monzonite porphyry.
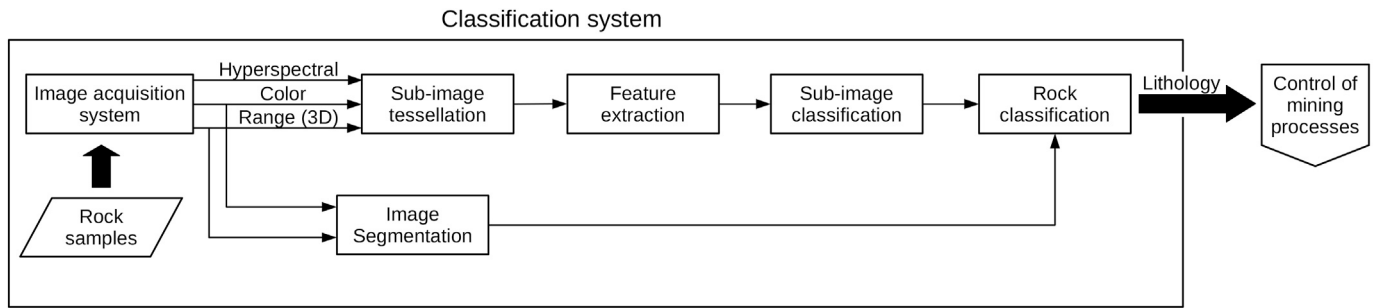
Classification system

Fig. 7. Block Diagram of the proposed lithological classification method.

in the images are also segmented in order to perform the final rock classification using their contour information. In this classification, a voting process is performed among the sub-images of each rock to classify the rock lithology. This second classification improves the performance of the method.

4.1. Rock segmentation

The resolution of the hyperspectral images is lower than the resolution of the range and color images. Therefore the range and color images were used in the segmentation to achieve a better result. The segmentation approach presented in our previous work [19] was used. The range images are segmented first because it is easier to identify every rock in these images. The range image segmentation is based on morphological operators, the seed growing algorithm [45,46], the watershed algorithm [47], and on the edge analysis from the connected elements obtained by the watershed algorithm. Then, the range image segmentation was used as a starting point in segmenting the color images. The color image segmentation is based on morphological operators, bilateral filtering [48], the watershed algorithm [47], and on an ad-hoc analysis of connected elements. Because the four types of images are registered, the segmentation is valid for all of them.

Fig. 8(a) and (b) show examples of the range and color image segmentations, respectively.

4.2. Feature extraction

The registered hyperspectral, color, and range images, are tessellated into sub-images, in a way similar to that proposed in Ref. [4]. The sub-images are squares of 60×60 pixels in the color image which is the
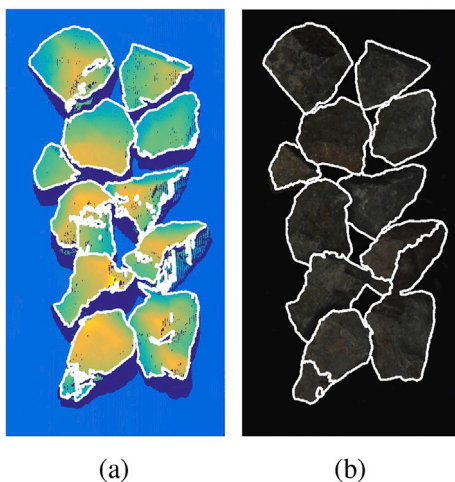
image type with the highest resolution. All features are computed within each sub-image. In the color and range images, we compute features based on Gabor filters and Local Binary Patterns (LBP). Some textures have particular orientations and features with rotation invariance are therefore considered (G_{rea} and BRINT_CS_CM [19]). In the color images, the features are computed in each channel of the HSV color space. The selected texture features are the best evaluated features reported in our previous publication [19]. In the color images these features provide information about the visual texture of the rock samples; and in the range images provide information about the 3D texture in the surface of the rocks. For example, when a rock fractures, the produced texture in the surface of the fracture (roughness, smoothness, flatness, etc.) is related to the lithology of the rock. In the hyperspectral images, the mean and standard deviation inside each channel for each sub-image are used as features. The features computed in the same sub-images from the different sensors were concatenated to build a feature vector. Table 1 shows the length of the feature vector when the different features are concatenated. A feature selection method was also used to reduce the number of features.

4.2.1. Gabor features

Gabor filters extract features with a particular spatial frequency and orientation. In this work we use Gabor filters computed using 5 scales, ν, and 8 orientations, μ. In order to extract the Gabor features, a convolution between the Gabor filters and the sub-images is performed, i.e.,

$$G_{\mu,\nu,i}(x,y) = \Psi_{\nu,\mu} * I_i, \tag{2}$$

where I_i is the sub-image i of image I. $G_{\mu,\nu,i}(x,y)$ are complex numbers and can be represented by their magnitude $M_{\mu,\nu,i}(x,y) = |G_{\mu,\nu,i}|$ and phase $\Phi_{\mu,\nu,i}(x,y) = \arg(G_{\mu,\nu,i})$. The magnitude $M_{\mu,\nu,i}$ provides information about the present frequencies, and the gradient of the phase $\mathscr{G}_{\mu,\nu,i}(x,y) = \nabla(\Phi_{\mu,\nu,i})$ provides information about how these frequencies change.

The same Gabor features with the best performance in Ref. [19], named G_{rea}, were used in this work. The G_{rea} features use the mean and the standard deviation of the magnitude inside each sub-image, $\overline{M_{\mu,\nu,i}}$ and $std(M_{\mu,\nu,i})$, respectively; and the mean and the standard deviation of the gradient, $\overline{\mathscr{G}_{\mu,\nu,i}}$ and $std(\mathscr{G}_{\mu,\nu,i})$, respectively. These features take scale and orientation into account. In order to consider rotation invariance, the features are rearranged according to a reference angle. The mean of $\overline{M_{\mu,\nu,i}}$ is computed across the scales in every orientation, and the orientation μ^{max} with maximum value is taken as the reference angle:

(a)   (b)

Fig. 8. Segmentation of range and color images. (a) Range image segmentation. (b) Color image segmentation. (For interpretation of the references to color in this figure legend, the reader is referred to the Web version of this article.)

Table 1
Number of features when the range, color and hyperspectral features are concatenated.

Range and Color img. Features	Hyperspectral img. Features	Number of Features
–	Mean + std	2424
BRINT_CS_CM + G_{rea}	–	1440
BRINT_CS_CM + G_{rea}	Mean + std	3864

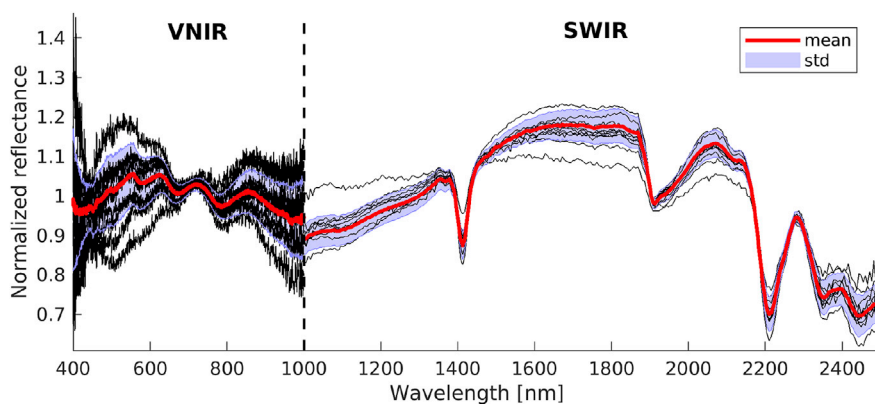$$\mu_i^{max} = arg\ max_\mu \sum_{i=0}^{4} \overline{M_{\mu,\nu,i}}. \tag{3}$$

The features $\overline{M_{\mu,\nu,i}}$, std($M_{\mu,\nu,i}$), $\overline{\mathscr{G}_{\mu,\nu,i}}$ and std($\mathscr{G}_{\mu,\nu,i}$) are then rearranged according to μ_i^{max} and used in the classification process. The G_{rea} features are represented by a vector of length 160 for each channel of the processed sub-image. Therefore, the G_{rea} vectors of a range and color sub-images are of length 160 and 480, respectively.

4.2.2. Local binary pattern features

The LBP features use binary comparisons between neighboring pixels by sampling around each pixel, generating a binary code in each neighborhood to characterize the texture [49]. The LBP features are extracted for each sub-image, building a histogram of all the binary codes resulting from the LBP codes within each sub-image. We chose to implement the BRINT_CS_CM (Binary Rotation Invariant and Noise Tolerant_CS_CM) LBP feature, because it achieved the best performance in our previous work [19]. The BRINT_CS_CM LBP was proposed in Ref. [50], and is computed by using three types of LBPs: BRINT_S (BRINT_Sign), BRINT_M (BRINT_Magnitude), and BRINT_C (BRINT_Center). Other properties of this LBP feature is that it is invariant under rotation, includes local thresholds, and has an average from the sampling of pixels in the neighborhood to achieve more robustness. The BRINT_CS_CM features were computed using 8 neighbors and 5 scales ([19]). The BRINT_CS_CM features are represented by a vector of length 200 for each channel of the processed sub-image.

4.2.3. Hyperspectral features

Because of the large number of channels available in the hyperspectral images, it was not necessary to compute texture features as is the case with color and laser images. The spectral signature of a lithology is a combination of the spectral signatures of the minerals present in the rock [51]. In order to remove the brightness variations, the spectra were normalized by dividing the spectrum in each pixel by its mean. Fig. 9 shows ten random examples of the normalized spectral signatures acquired for various pixels of one sub-image. Some of these spectral signatures are different from each other because they show the reflectance of the different grains of minerals that form the rock. Fig. 9 also shows the mean reflectance of each channel of the hyperspectral sub-image and its standard deviation. This mean reflectance can be considered the spectral signature of the lithology, and it is similar among different sub-images of rocks of the same lithology. Fig. 10 shows examples of the mean spectra of the different lithologies. Each curve represents the mean spectrum along the sub-images of one image of the lithology. Reflectance values are offset from origin for clarity, and the VNIR and SWIR spectra are concatenated. For a better visualization, the offsets of the VNIR and SWIR spectra are different in order to match the reflectance of both curves. The mean reflectance and its standard deviation in each channel of the hyperspectral sub-images were therefore the hyperspectral features used for lithological

classification. Since the bordering channels of the hyperspectral images are noisy, a range of the central channels is considered. In the VNIR images, the 944 channels from 399.51 to 1000.06 nm are used. In the SWIR images, the 268 channels from 1000.21 nm to 2499.26 nm are used. Hence, 2424 hyperspectral features are computed in each sub-image. Fig. 11 shows the mean spectra and mean standard deviations of two lithologies, computed in 500 sub-images.

We also studied the reduction of the number of hyperspectral features for sub-image classification. First, the performance obtained by using only the VNIR or SWIR portions of the spectrum was studied. Then, a feature reduction method was used with the features computed in the full spectrum (both VNIR and SWIR). A method for reducing the number of features, such as PCA, performs a transformation of the full feature space which, in our case, is associated with the hyperspectral wavelengths. Nevertheless, our aim is to analyze the best hyperspectral wavelengths for lithological classification. The identification of these wavelengths makes it possible to avoid the computation and acquisition of non-relevant wavelengths when the method is used for online classification. Hence, the CMIM feature selection method [52–55] was chosen. The CMIM method is based on mutual information [56,57]. This method selects relevant features, avoids redundancy, and includes feature complementarity. In each iteration of the CMIM method, the features that maximize the mutual information with the class to be predicted are selected, given each one of the features already selected separately. The CMIM method assumes that a feature is relevant when it provides more significant information of the class, and if this information is not already contained in the other selected features [58].

4.3. Classification

The rock type classification is performed following two stages in cascade, sub-image classification, and rock contour classification as follows:

4.4. Classification by sub-images

The state-of-the-art SVM classifier was used to achieve the best performance of the proposed method. The SVM is a very popular classification method because of its excellent results in many different fields. Linear and nonlinear SVMs were tested for classification. The publicly available LibSVM [59] was used for the implementation of the nonlinear classifier. A C—SVC SVM was used to classify the sub-images [60]. Using a non-linear transformation, the SVM maps the input vectors to a high-dimensional space where linear decision hyperplanes are constructed to separate the classes. The kernel functions to map the input vector were the RBF (radial basis functions), ($K(u, v) = exp(-\gamma^* |u - v|^2)$). The publicly available LIBLINEAR [61] library was used for the linear classifier. The one-versus-one multi-classification strategy was used in the linear and nonlinear SVM classifiers. The regularization

Fig. 9. VNIR and SWIR mean spectrum of one sub-image. The black curves represent the spectra of 10 pixels randomly chosen in a sub-image. The red line and the blue stripe are the mean spectrum of the sub-image and its standard deviation, respectively. The VNIR and SWIR spectra do not match at 1.000 nm Because they were acquired with different cameras which have different sensitivities. (For interpretation of the references to color in this figure legend, the reader is referred to the Web version of this article.)
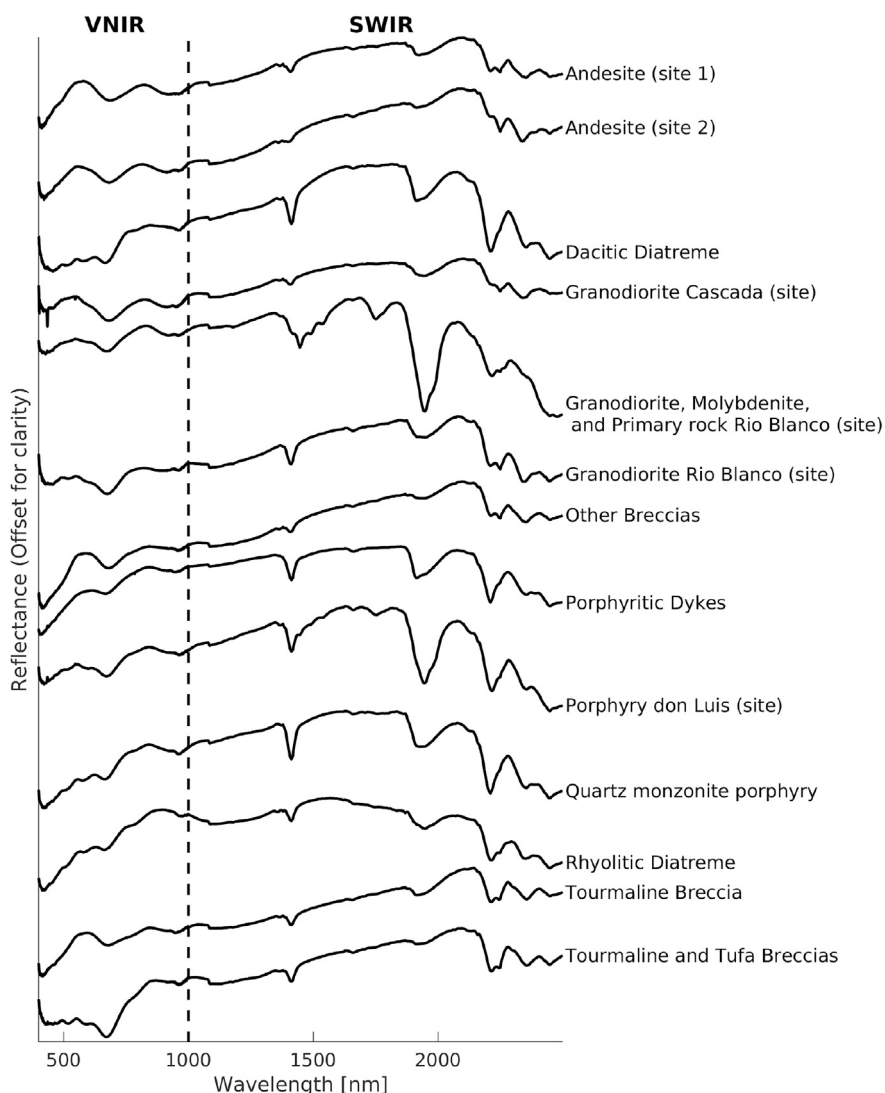
Fig. 10. Examples of the spectra of different lithologies. The curves show the mean spectrum computed on one image of each lithology. Reflectance values are offset to match the VNIR and SWIR spectra which are acquired with different sensors in order to have a better visualization.
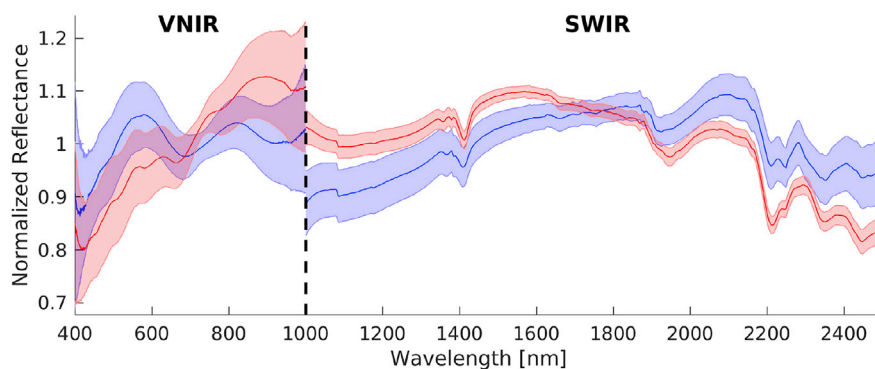

Fig. 11. VNIR and SWIR spectra of two lithologies. The curves and stripes represent the mean spectrum and the mean standard deviation of the spectrum of two different lithologies. The means were computed using 500 sub-images for each lithology.

parameter *C* of the linear and nonlinear SVMs [59], and the parameter γ for the radial basis functions of the nonlinear SVM were obtained by searching in a training subset of the data which contained 3% of the data.

A cross validation procedure, and a test set were used to measure the performance of the proposed method. To do so, the database was divided into a cross validation set, and a test set. The cross validation set was divided into subsets. In each iteration of the cross validation, one subset was used as the validation set and the others as the training sets. Only sub-images with more than 90% rock area are classified. The sub-images with background that are not used for training are detected using the color image segmentation. The classifiers trained in each iteration of the cross validation were also evaluated in the test set.

4.5. Classification by rock contour

As described in Refs. [15,16], the classification by rock contour allows correcting errors in classifying individual rock sub-images into rock type classes. The classification of rock sub-images is based on features extracted from each sub-image alone, and, using the rock contour information, the rock classification is improved. This can be performed by using a voting process with all the sub-images that belong to a single rock. The color and range image segmentation is used to identify the contour of the rocks and the sub-images that are inside them. Then, the most frequent lithology in the sub-images within each rock contour assigns its class to all the sub-images within the contour. Therefore, if the percentage of sub-images within a rock contour is over a confidence threshold, all the sub-images of the rock are assigned to this lithology class. This voting process improves the performance of the final classification because it corrects some misclassified sub-images [15,16].

5. Experiments

The 90% of the database (18 images of each rock type) was used as cross validation set and 10% (2 images of each rock type) was reserved as test set. The cross validation set was divided into 9 subsets, and a leave-one-out cross validation scheme was used to perform the experiments. In each iteration, 8 subsets were used for training and one for validation. To carry out a balanced training of the classifier, the same number of training examples of each class were used in each iteration. In each experiment, the parameters of the SVM were determined by searching on a grid with a logarithmic scale using a 5-fold cross validation in a subset of the training set. The values of the grid were in the range $log_2(C) = [0, 35]$ and $log_2(\gamma) = [-20, -6]$ for C and γ, respectively. We used a step of length 2, and a fine-tuning was performed around the best value using a step of length 0.4. To search C and γ, 3% of the available sub-images were selected randomly. The best performance obtained with the SVMs was also compared with the performance achieved by using a random forest (RF) classifier. A RF classifier with 300 trees was used in the comparison. The classifiers trained in each iteration of the cross validation were then evaluated in the test set.

The classification performance was measured using the BRINT_CS_CM and G_{rea} features in the range and color images, and the hyperspectral features (mean + std) in the hyperspectral VNIR and SWIR images.

The method was implemented in MATLAB R2015 for training and testing. A personal computer with Ubuntu 16.1 (64 bits), equipped with an Intel Core i7-7700 CPU @ 3.6 GHz × 8 processor, and 64 GB RAM was used to run the method.

6. Results

Table 2 shows the classification performance obtained by using the various range, color, and hyperspectral features with the linear and nonlinear (RBF) SVM classifiers. It is important to note that the sub-image classification assesses the performance of each type of feature, and the rock classification is guided by the rock segmentation. In order to verify the statistical significance ($p < 0.05$) of the differences among the classification performances, an analysis of variance (ANOVA), and a multiple comparison test were carried out. The Fisher's least significant difference procedure was used in the multiple comparison test. In the validation and test sets, the performances obtained in sub-image classification by using the different features have statistical differences among them. Nevertheless, the use of a linear or nonlinear classifier only produces a statistically significant difference if the color and range features are used exclusively. The performances obtained in the rock classification of the validation and test set, using only color and range features with linear or nonlinear classifiers, are the only ones that are statistically different from the rest. Table 2 shows that the best performance for sub-image classification was achieved using only the hyperspectral features. The classification performances obtained in the test set using only the hyperspectral features were 98.62% and 99.95% in the sub-image and rock classification, respectively. Table 1 shows the length of the feature vectors used in each experiment. The largest feature vector is produced when the hyperspectral, range, and color images are used together. In this vector, 62.7% of the elements are hyperspectral features and 37.2% of the elements are texture features computed in the color and range images. Although most of the features are hyperspectral features, the performance in this case is lower than the performance obtained by using only the hyperspectral features (length 2424). The reason behind this result may be that the texture features are noisy. In fact, the performance obtained in the test set by using only texture features is the lowest, 56.86% in the sub-image classification. Table 2 also shows the performance obtained by using a RF classifier and the features with which the best performance in the SVM classification was achieved, the hyperspectral features. The performances obtained by using a RF were lower than those achieved by the linear and non-linear SVMs, in both the validation and test sets.

Table 3 shows the classification performance obtained by using only the VNIR or the SWIR portion of the spectrum with the linear or nonlinear classifier. These results were compared with the performance obtained by using the full spectrum (Table 2). In the sub-image classification of the test set, the performances obtained by using the full spectrum with the linear or nonlinear classifier are the only ones that do not have a statistical difference between them. In the sub-image classification of the validation set, these performances are not statistically different from the one obtained using the SWIR spectrum and the nonlinear classifier. The performances obtained in the rock classification of the validation set are not statistically different. Nevertheless, the performances obtained using the VNIR spectrum in the test set are statistically different from the others and between themselves. The results show that the best

Table 2

Percentage of correct sub-image classification considering various types of features in the color, range, and hyperspectral images. The table shows the results obtained by using a nonlinear SVM with RBF as kernel functions, and a linear SVM. The result obtained by using a RF classifier, on the features with which the best performance was achieved in the classification by SVMs, is also included. These classifiers were used for the sub-image classification, and then the classification was improved by using voting among sub-images within each rock. The symbol "–" means that none of the features were used. The results show the [mean]±[standard deviation].

Range and Color img. Features	Hyperspectral img. Features	Sub-image classification			Rock classification		
		Training set	Validation set	Test set	Training set	Validation set	Test set
SVM (RBF)							
–	Mean + std	99.90 ± 0.01	97.91 ± 1.42	98.62 ± 0.10	100.00 ± 0.00	99.29 ± 1.50	99.95 ± 0.01
BRINT_CS_CM + G_{rea}	–	100.00 ± 0.00	59.38 ± 2.33	61.10 ± 0.57	100.00 ± 0.00	86.74 ± 4.95	90.26 ± 1.44
BRINT_CS_CM + G_{rea}	Mean + std	100.00 ± 0.00	94.33 ± 0.65	94.09 ± 0.50	100.00 ± 0.00	99.53 ± 0.49	99.26 ± 0.35
SVM (Linear)							
–	Mean + std	100.00 ± 0.00	97.68 ± 1.49	98.46 ± 0.10	100.00 ± 0.00	99.28 ± 1.51	99.95 ± 0.00
BRINT_CS_CM + G_{rea}	–	72.76 ± 0.52	55.32 ± 1.14	56.86 ± 0.98	96.75 ± 0.29	83.93 ± 1.75	84.86 ± 2.01
BRINT_CS_CM + G_{rea}	Mean + std	99.88 ± 0.04	94.59 ± 0.53	94.30 ± 0.24	100.00 ± 0.00	99.31 ± 0.33	99.39 ± 0.18
RF							
–	Mean + std	100.00 ± 0.00	84.95 ± 1.08	83.77 ± 0.24	100.00 ± 0.00	96.88 ± 0.62	96.68 ± 0.35

Table 3

Percentage of correct sub-image classification considering hyperspectral features computed in the VNIR or SWIR portions of the spectrum. The table shows the results obtained by using a nonlinear SVM with RBF as kernel functions, and a linear SVM. These classifiers were used for the sub-image classification, and then the classification was improved by using voting among sub-images within each rock. The symbol "–" means that none of the features were used. The results show the [mean]± [standard deviation].

Hyperspectral img. type	Sub-image classification			Rock classification		
	Training set	Validation set	Test set	Training set	Validation set	Test set
SVM (RBF)						
VNIR	95.77 ± 0.09	87.07 ± 1.64	85.78 ± 0.49	99.95 ± 0.03	98.28 ± 1.61	98.11 ± 0.42
SWIR	98.91 ± 0.08	96.76 ± 1.48	97.42 ± 0.09	99.90 ± 0.03	99.46 ± 1.24	99.91 ± 0.06
SVM (Linear)						
VNIR	96.43 ± 0.69	84.26 ± 1.89	83.25 ± 0.32	99.94 ± 0.07	98.11 ± 1.63	99.08 ± 0.51
SWIR	99.18 ± 0.40	96.26 ± 1.39	96.76 ± 0.32	99.92 ± 0.09	99.37 ± 1.36	99.75 ± 0.29

performance is achieved by using the full spectrum, and that the use of a linear or nonlinear classifier does not affect this performance. The performances obtained by using the SWIR spectrum are similar to those obtained by using the full spectrum. The worst results were obtained by using only the VNIR spectrum. The number of hyperspectral features used can be even further reduced without a loss in performance, as shown below.
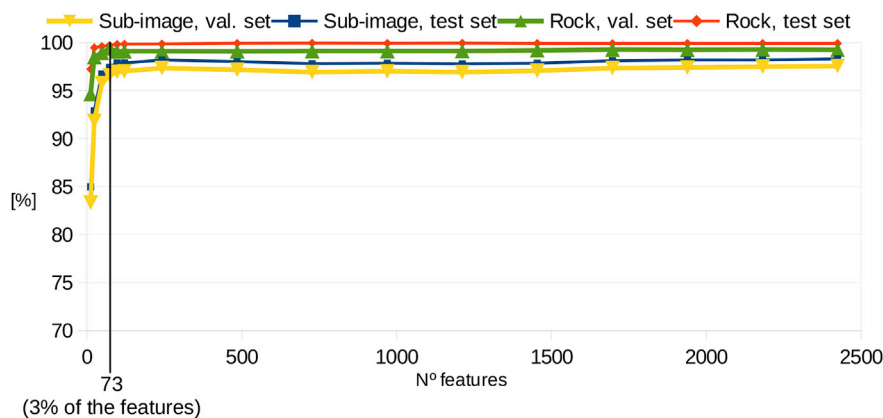
Fig. 12 shows the classification performance obtained in the validation and test sets using the hyperspectral features when the number of features is reduced by the CMIM method. A linear SVM was used in the sub-image classification. The figure shows that even if only 3% of the features are used (73 features), a performance of over 99% accuracy is achieved in the rock classification, and over 97% in the sub-image classification. This result is very important because it allows a reduction in the number of computations by ignoring 97% of the extracted features without significantly affecting classification performance. This reduction in the number of required features has a direct impact on the computational time required to implement and operate a rock type classification system. Fig. 12 shows that if a reduction in the performance is accepted, using only 2% (48 features) of the hyperspectral features, classification performances of over 99% and over 96% are achieved in the rock and sub-image classifications, respectively. Fig. 13 shows the hyperspectral features selected as the number of features is reduced using the CMIM method. Fig. 13 shows that if only a small number of features are selected, the mean is preferred to the standard deviation as feature. The selected wavelengths do not follow a strong pattern, but there are some preferred wavelengths close to 500, 1400, 1900, 2200 and 2400 nm. It is important to note that the wavelengths selected in the visual spectrum (from 400 to 750 nm) provide more information about the spectra of the lithologies in this range than the color images, which only provide the sum of the spectral response of the sensor centered at three positions of the spectrum (red, green, blue). Fig. 14 shows the mean-centered spectra of the different lithologies (see Fig. 10), and the wavelengths used if 3%

of the features are selected by the CMIM method. Most of the selected wavelengths are in bands that match some minima of the spectra, or absorption features. The chemical composition of the rock samples is related to these minima [62]. In general, the minima near 1400 nm are related to absorption due to the presence of OH/H_2O. The minima near 1900 nm are related to the presence of OH/H_2O and CO_3; and the minima near 2200 and 2400 nm are related to the presence of mica, OH, and CO_3. The different chemical compositions of these rocks are the result of their formation and subsequent metamorphism.

7. Conclusions

Automatic rock characterization will be needed at many different stages of future mine operations, and used to supervise and optimize different processes in the laboratory as well as at mine locations for mine planning and exploitation. The lithology of the rocks processed at a mining plant can be very useful, for example, in mine planning or in controlling the grinding process. The lithology provides information about the chemical composition of the rock, and its physical properties. In this paper we propose a new method for rock lithological classification using range, color, and hyperspectral images, which, according to our literature review, is the first method that uses a combination of these types of images to perform lithological classification of rocks. Our study shows that the classification is improved significantly by using hyperspectral information from rocks (from 90.26% to 99.95% in rock classification).

The classification method is divided into two stages. First the images are tessellated into sub-images which are classified by an SVM, using features computed within each sub-image. In the second stage, each rock is classified using a voting process among the sub-images that belong to the same rock. This second stage improves the classification performance significantly. The rocks are identified by performing a segmentation based on range and high resolution color images. The range 3D

Fig. 12. Classification performance of the hyperspectral features as the number of features is reduced. The CMIM method was used to select the most relevant features, and a linear SVM was used in the sub-image classification. The graph shows the results of the sub-image and rock classifications in the validation and test sets.
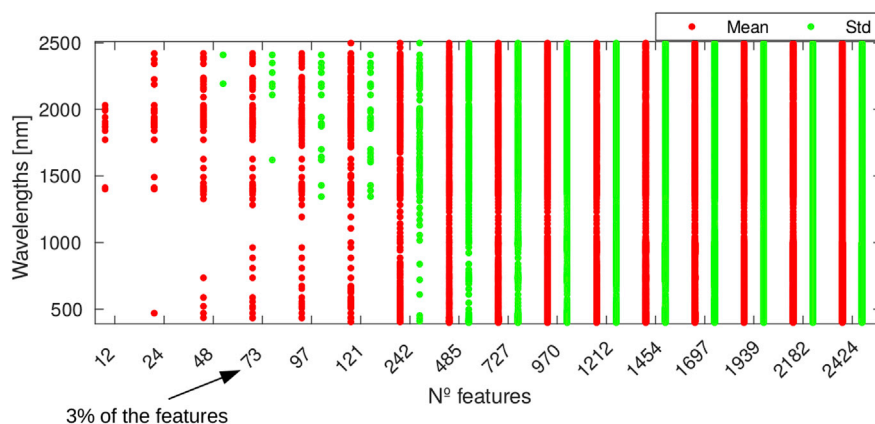
Fig. 13. Hyperspectral features selected as the number of features is reduced using the CMIM method. The graph shows the wavelengths (channels of the hyperspectral images) selected to compute the mean and the standard deviation as hyperspectral features.
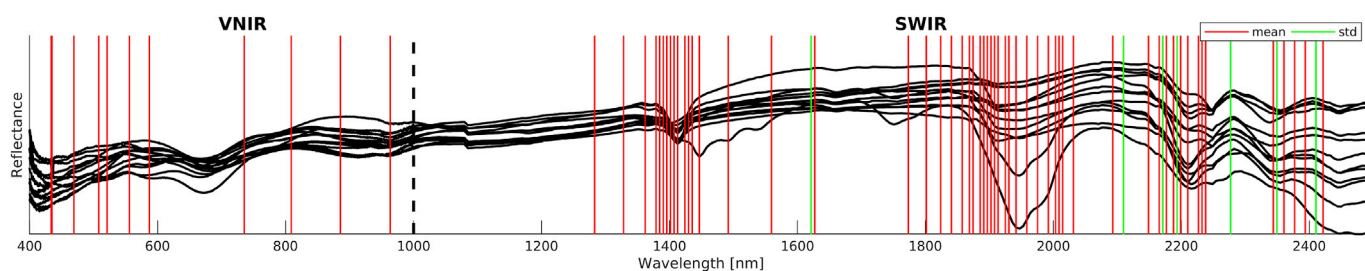

Fig. 14. Wavelengths (channels of the hyperspectral images) used to compute the 73 hyperspectral features selected when the number of features is reduced to 3% using the CMIM method. The black curves represent the mean-centered spectra of the different lithologies.

information improves rock segmentation even if their colors and textures are similar to the surrounding rocks. The experiments were performed using a database with 13 different lithologies from a copper mine in Chile.

In the color and range images, the best evaluated features reported in our previous publication [19] were used. In the hyperspectral images, the mean and standard deviation inside each channel of the sub-image were used as features. The performances obtained by using the various features were measured dividing the database into a tow set: a set to perform a leave-one-out 9-fold cross validation, and a set for testing. The best classification performance was achieved by using only the hyperspectral features (99.95%). The CMIM feature selection method was used to analyze the number of features needed for classification. The result obtained, 99.73% accuracy in test set using only 3% of the features, was not significantly different from that obtained using all the features. This method allowed a reduction in the number of features from 2424 to 73 with no significant loss in classification performance. This reduction in the number of features makes it possible to reduce the computational time required to operate a rock type classification system. Furthermore, this reduction is very important because a multispectral imaging system could be used for classification instead of a hyperspectral one, because it is cheaper and easier to implement for on-line applications [24,26]. The high accuracy in lithological classification obtained justifies real applications of this method in industry which will be our next step.

Acknowledgments

References

[1] A. Casali, G. Gonzalez, G. Vallebuona, C. Perez, R. Vargas, Grindability soft-sensors based on lithological composition and on-line measurements, Miner. Eng. 14 (7) (2001) 689–700.

[2] S. Chatterjee, A. Bhattacherjeeb, B. Samanta, S.K. Pal, Image-based quality monitoring system of limestone ore grades, Comput. Ind. 61 (5) (2010) 391–408.

[3] O. Guyot, T. Monredon, D. LaRosa, A. Broussaud, Visiorock, an integrated vision technology for advanced control of comminution circuits, Miner. Eng. 17 (11–12) (2004) 1227–1235.

[4] J. Tessier, C. Duchesne, G. Bartolacci, A machine vision approach to on-line estimation of run-of-mine ore composition on conveyor belts, Miner. Eng. 20 (12) (2007) 1129–1144.

[5] C. Perez, A. Casali, G. Gonzalez, G. Vallebuona, R. Vargas, Lithological composition sensor based on digital image feature extraction, genetic selection of features and neural classification, in: 1999 International Conference on Information Intelligence and Systems, IEEE, 1999, pp. 236–241. Bethesda, Maryland, USA.

[6] P. Paclík, S. Verzakov, R.P.W. Duin, Improving the maximum-likelihood cooccurrence classifier: a study on classification of inhomogeneous rock images, in: H. Kalviainen, J. Parkkinen, A. Kaarna (Eds.), Image Analysis, Vol. 3540 of Lecture Notes in Computer Science, Springer Berlin Heidelberg, 2005, pp. 998–1008.

[7] L. Lepistö, I. Kunttu, J. Autio, A. Visa, Rock image classification using color features in gabor space, J. Electron. Imaging 14 (4).

[8] V. Singh, S.M. Rao, Application of image processing in mineral industry: a case study of ferruginous manganese ores, Miner. Process. Extr. Metall. (IMM Trans. Sect. C) 115 (3) (2006) 155–160.

[9] T. Kachanubal, S. Udomhunsakul, Rock textures classification based on textural and spectral features, Int. J. Comp. Elec. Auto. Cont. Info. Eng. 2 (4) (2008) 658–664.

[10] L.B. Gonçalves, F.R. Leta, S. de C. Valente, Macroscopic rock texture image classification using an hierarchical neuro-fuzzy system, in: 16th International Conference on Systems, Signals and Image Processing, IWSSIP, 2009, 2009, 2009.

[11] S. Chatterjee, S. Bandopadhyay, D. Machuca, Ore grade prediction using a genetic algorithm and clustering based ensemble neural network model, Math. Geosci. 42 (3) (2010) 309–326.

[12] N. Singh, T.N. Singh, A. Tiwary, K.M. Sarkar, Textural identification of basaltic rock mass using image processing and neural network, Comput. Geosci. 14 (2) (2010) 301–310.

[13] A. Fernández, O. Ghita, E. González, F. Bianconi, P.F. Whelan, Evaluation of robustness against rotation of LBP, CCR and ILBP features in granite texture classification, Mach. Vis. Appl. 22 (6) (2011) 913–926.

[14] N.A.M. Isa, Z.M. Sani, M.S. Al-Batah, Automated intelligent real-time system for aggregate classification, Int. J. Miner. Process. 100 (1–2) (2011) 41–50.

[15] C.A. Perez, P.A. Estévez, P.A. Vera, L.E. Castillo, C.M. Aravena, D.A. Schulz, L.E. Medina, Ore grade estimation by feature selection and voting using boundary detection in digital image analysis, Int. J. Miner. Process. 101 (1–4) (2011) 28–36.

[16] C.A. Perez, J.A. Saravia, C.F. Navarro, D.A. Schulz, C.M. Aravena, F.J. Galdames, Rock lithological classification using multi-scale gabor features from sub-images, and voting with rock contour information, Int. J. Miner. Process. 144 (2015) 56–64.

[17] F. Bianconi, E. González, A. Fernández, S.A. Saetta, Automatic classification of granite tiles through colour and texture features, Expert Syst. Appl. 39 (12) (2012) 11212–11218.

[18] A.K. Patel, S. Chatterjee, Computer vision-based limestone rock-type classification using probabilistic neural network, Geosci. Front. 7 (1) (2016) 53–60.

[19] F.J. Galdames, C.A. Perez, P.A. Estévez, M. Adams, Classification of rock lithology by laser range 3D and color images, Int. J. Miner. Process. 160 (2017) 47–57.

[20] S. Serranti, A. Gargiulo, G. Bonifazi, Classification of polyolefins from building and construction waste using nir hyperspectral imaging system, Resour. Conserv. Recycl. 61 (0) (2012) 52–58.

[21] A. Ulrici, S. Serranti, C. Ferrari, D. Cesare, G. Foca, G. Bonifazi, Efficient chemometric strategies for PET-PLA discrimination in recycling plants using hyperspectral imaging, Chemometr. Intell. Lab. Syst. 122 (0) (2013) 31–39.

[22] R. Gosselin, D. Rodrigue, C. Duchesne, A hyperspectral imaging sensor for on-line quality control of extruded polymer composite products, Comput. Chem. Eng. 35 (2) (2011) 296–306.

[23] D. Ye, L. Sun, W. Tan, W. Che, M. Yang, Detecting and classifying minor bruised potato based on hyperspectral imaging, Chemometr. Intell. Lab. Syst. 177 (15) (2018) 129–139.

[24] W. Huang, J. Li, Q. Wang, L. Chen, Development of a multispectral imaging system for online detection of bruises on apples, J. Food Eng. 146 (2015) 62–71.

[25] R. Calvini, A. Ulrici, J.M. Amigo, Practical comparison of sparse methods for classification of arabica and robusta coffee species using near infrared hyperspectral imaging, Chemometr. Intell. Lab. Syst. 146 (15) (2015) 503–511.

[26] R. Calvini, J.M. Amigo, A. Ulrici, Transferring results from NIR-hyperspectral to NIR-multispectral imaging systems: a filter-based simulation applied to the classification of Arabica and Robusta green coffee, Anal. Chim. Acta 967 (2017) 33–41.

[27] F.D. van der Meer, H.M.A. van der Werff, F.J.A. van Ruitenbeek, C.A. Hecker, W.H. Bakker, M.F. Noomen, M. van der Meijde, E.J.M. Carranza, J.B. de Smeth, T. Woldai, Multi- and hyperspectral geologic remote sensing: a review, Int. J. Appl. Earth Obs. Geoinf. 14 (1) (2012) 112–128.

[28] E. Pirard, Multispectral imaging of ore minerals in optical microscopy, Mineral. Mag. 68 (2) (2004) 323–333.

[29] W. Li, E.W. Tramel, S. Prasad, J.E. Fowler, Nearest regularized subspace for hyperspectral classification, IEEE Trans. Geosci. Remote Sens. 52 (1) (2014) 477–489.

[30] W. Li, Q. Du, Gabor-filtering-based nearest regularized subspace for hyperspectral image classification, IEEE J. Selected Topics. App. Earth Obser. Remote Sens. 7 (4) (2014) 1012–1022.

[31] Z. Wang, N.M. Nasrabadi, T.S. Huang, Semisupervised hyperspectral classification using task-driven dictionary learning with laplacian regularization, IEEE Trans. Geosci. Remote Sens. 53 (3) (2015) 1161–1173.

[32] C. Li, Y. Ma, X. Mei, C. Liu, J. Ma, Hyperspectral image classification with robust sparse representation, IEEE Geosci. Remote Sens. Lett. 13 (5) (2016) 641–645.

[33] S. Yu, S. Jia, C. Xu, Convolutional neural networks for hyperspectral image classification, Neurocomputing 219 (5) (2017) 88–98.

[34] J. Yang, Y.-Q. Zhao, J.C.-W. Chan, Learning and transferring deep joint spectral-spatial features for hyperspectral classification, IEEE Trans. Geosci. Remote Sens. 55 (8) (2017) 4729–4742.

[35] Z. He, Y. Wang, J. Hu, Joint sparse and low-rank multitask learning with laplacian-like regularization for hyperspectral classification, Rem. Sens. 10 (2) (2018) 322.

[36] Z. He, J. Li, K. Liu, L. Liu, H. Tao, Kernel low-rank multitask learning in variational mode decomposition domain for multi-/hyperspectral classification, IEEE Trans. Geosci. Remote Sens. 56 (7) (2018) 4193–4208.

[37] G.R. Taylor, Mineral and lithology mapping of drill core pulps using visible and infrared spectrometry, Nat. Resour. Res. 9 (4) (2000) 257–268.

[38] P.-S. Ross, A. Bourke, B. Fresia, A multi-sensor logger for rock cores: methodology and preliminary results from the matagami mining camp, Canada, Ore Geol. Rev. 53 (0) (2013) 93–111.

[39] J.F. Huntington, A.J. Mauger, R.G. Skirrow, E.N. Bastrakov, P. Connor, P. Mason, J.L. Keeling, D.A. Coward, M. Berman, R. Phillips, L.B. Whitbourn, P.S. Heithersay, Automated mineralogical core logging at the Emmie Bluff iron oxide copper-gold prospect, MESA 41 (2006) 38–44.

[40] J. Huntington, L. Whitbourn, P. Mason, M. Berman, M.C. Schodlok, Hylogging–voluminous industrial-scale reflectance spectroscopy of the earth's subsurface, in: Proceedings of ASD and IEEE GRS; Art, Science and Applications of Reflectance Spectroscopy Symposium, vol. 2, 2010, p. 14. Boulder, Colorado, USA.

[41] M. Tappert, B. Rivard, D. Giles, R. Tappert, A. Mauger, Automated drill core logging using visible and near-infrared reflectance spectroscopy: a case study from the Olympic Dam IOCG deposit, South Australia, Econ. Geol. 108 (2013) 483–494.

[42] J. Burger, P. Geladi, Hyperspectral NIR image regression part i: calibration and correction, J. Chemom. 19 (5–7) (2005) 355–363.

[43] E. Rublee, V. Rabaud, K. Konolige, G. Bradski, ORB: an efficient alternative to SIFT or SURF, in: 2011 International Conference on Computer Vision, Barcelona, Spain, 2011, pp. 2564–2571.

[44] S. Leutenegger, M. Chli, R.Y. Siegwart, BRISK: binary robust invariant scalable keypoints, in: 2011 International Conference on Computer Vision, Barcelona, Spain, 2011, pp. 2548–2555.

[45] M.J. Thurley, K.C. Ng, Identifying, visualizing, and comparing regions in irregularly spaced 3D surface data, Comput. Vis. Image Understand. 98 (2) (2005) 239–270.

[46] M.J. Thurley, T. Andersson, An industrial 3D vision system for size measurement of iron ore green pellets using morphological image segmentation, Miner. Eng. 21 (5) (2008) 405–415.

[47] S. Beucher, C. Lantuéjoul, Use of watersheds in contour detection, in: International Workshop on Image Processing: Real-Time Edge and Motion Detection/Estimation, Rennes, France, 1979, pp. 17–21.

[48] K.N. Chaudhury, Acceleration of the shiftable O(1) algorithm for bilateral filtering and non-local means, IEEE Trans. Image Process. 22 (4) (2013) 1291–1300.

[49] T. Ojala, M. Pietikäinen, T. Mäenpää, Multiresolution gray-scale and rotation invariant texture classification with local binary patterns, IEEE Trans. Pattern Anal. Mach. Intell. 24 (7) (2002) 971–987.

[50] L. Liu, Y. Long, P.W. Fieguth, S. Lao, G. Zhao, BRINT: binary rotation invariant and noise tolerant texture classification, IEEE Trans. Image Process. 23 (7) (2014) 3071–3084.

[51] Y. Guo, M. Berman, A comparison between subset selection and l1 regularisation with an application in spectroscopy, Chemometr. Intell. Lab. Syst. 118 (15) (2012) 127–138.

[52] F. Fleuret, Fast binary feature selection with conditional mutual information, J. Mach. Learn. Res. 5 (2004) 1531–1555.

[53] G. Wang, F.H. Lochovsky, Feature selection with conditional mutual information MaxiMin in text categorization, in: Thirteenth ACM International Conference on Information and Knowledge Management, CIKM, New York, USA, 2004, pp. 342–349.

[54] I. Guyon, S. Gunn, M. Nikravesh, L.A. Zadeh (Eds.), Feature Extraction: Foundations and Applications, Studies in Fuzziness and Soft Computing, Springer-Verlag Berlin Heidelberg, 2006.

[55] G. Brown, A. Pocock, M.-J. Zhao, M. Luján, Conditional likelihood maximisation: a unifying framework for information theoretic feature selection, J. Mach. Learn. Res. 13 (2012) 27–66.

[56] P.A. Estevez, M. Tesmer, C.A. Perez, J.M. Zurada, Normalized mutual information feature selection, IEEE Trans. Neural Netw. 20 (2) (2009) 189–201.

[57] J.R. Vergara, P.A. Estévez, A review of feature selection methods based on mutual information, Neural Comput. Appl. 24 (1) (2014) 175–186.

[58] J.E. Tapia, C.A. Perez, K.W. Bowyer, Gender classification from the same iris code used for recognition, IEEE Trans. Inf. Forensics Secur. 11 (8) (2016) 1760–1770.

[59] C.-C. Chang, C.-J. Lin, LIBSVM: a library for support vector machines, ACM Transac. Intell. Sys. Technol. (TIST) 2 (3) (2011), 27–27.

[60] C. Cortes, V. Vapnik, Support-vector networks, Mach. Learn. 20 (3) (1995) 273–297.

[61] R.-E. Fan, K.-W. Chang, C.-J. Hsieh, X.-R. Wang, C.-J. Lin, LIBLINEAR: a library for large linear classification, J. Mach. Learn. Res. 9 (2008) 1871–1874.

[62] M. Berman, L. Bischof, R. Lagerstrom, Y. Guo, J. Huntington, P. Mason, A.A. Green, A comparison between three sparse unmixing algorithms using a large library of shortwave infrared mineral spectra, IEEE Trans. Geosci. Remote Sens. 55 (6) (2017) 3588–3610.